Journal of Power Sources 199 (2012) 53–60

Contents lists available at SciVerse ScienceDirect

Journal of Power Sources

journal homepage: www.elsevier.com/locate/jpowsour

Anodic properties of hollow carbon nanofibers for Li-ion battery

Byoung-Sun Lee [a], Seoung-Bum Son [a,b], Kyu-Min Park [a], Woong-Ryeol Yu [a,*], Kyu-Hwan Oh [a], Se-Hee Lee [b,c]

[a] Department of Materials Science and Engineering, Seoul National University, 599 Gwanangno, Gwanak-gu, Seoul 151-742, Republic of Korea
[b] Department of Mechanical Engineering, University of Colorado 427 UCB, Boulder, CO 80309, USA
[c] World Class University Hybrid Materials Program, Department of Materials Science and Engineering, Seoul National University, 599 Gwanangno, Gwanak-gu, Seoul 151-742, Republic of Korea

ARTICLE INFO

Article history:
Received 1 September 2011
Received in revised form 4 October 2011
Accepted 6 October 2011
Available online 14 October 2011

Keywords:
Hollow carbon nanofibers
Anodic properties
Thermal treatment
Turbostratic carbon structure

ABSTRACT

This work reports on hollow carbon nanofibers (HCNFs) as anode materials for Li-ion batteries. Various HCNFs are synthesized using co-axial electrospinning of styrene-*co*-acrylonitrile (core) and poly(acrylonitrile) (shell) solutions and subsequent thermal treatments. The microstructures of HCNFs are examined using SEM, Raman spectroscopy, WAXD, and HR-TEM. The effect of the carbonization temperature on their turbostratic carbon structures and electrochemical properties is systematically investigated. As the carbonization temperature increases, both crystallite thickness and length significantly increases while the initial irreversible capacity decreases. These predictable microstructure and electrochemical performance of HCNFs provide important insight for the design of novel nanostructured anode materials such as Si or Sn encapsulated HCNFs.

1. Introduction

In the last two decades, lithium-ion batteries (LIBs) have been mainly used as the main power source for portable electronic devices. High-energy-density and long-lasting LIBs are in high demand to power electric vehicles. There have been various attempts to improve the energy and power densities of LIBs by developing new materials, such as sulfur-based positive electrodes [1–3] and silicon or tin negative electrodes [4,5]. Silicon and Tin have been considered as promising anode materials due to their higher capacity than carbonaceous anode materials [6,7]. Their mechanical failure (pulverization), however, was unavoidable due to the large volume change exhibited during lithiation/delithiation, causing the loss of electrical contact [4,8,9]. In addition, sulfur-based cathodes have faced problems, such as low electric conductivity and volumetric changes during reactions [2]. To overcome these common problems of both novel cathode and anode materials, carbonaceous materials have been widely utilized as matrix materials accommodating novel cathode or anode materials, such that they mitigate the pulverization and compensate for the loss of electrical contact [2–4,10–15].

Since the conception of novel compositions of electrode materials and carbonaceous materials in early 2000s [16,17], various types of composite electrodes have been continuously suggested, including spherical zero-dimensional composites [3,18], tubular, or fibrous one-dimensional composites [4,9–12,15,19] and particles-in-matrix structured three-dimensional composites [20]. The main purpose of such studies on composite electrodes has been focused on maximizing the performances of electrodes by realizing theoretical capacities and/or connecting electric contacts using carbonaceous materials; however, the contribution of carbonaceous materials is still a considerable part of what determines the electrochemical performances of the composite electrodes. Nevertheless, recent studies including the aforementioned references have mostly dealt with the composition effects of novel electrode materials. Indeed, the electrochemical performances of various carbonaceous bulky (i.e. larger than micron size) materials have been widely investigated from the middle of the 1990s to the early 2000s [21–27], but the performances of submicron sized carbonaceous materials should be investigated with respect to the discontinuity of material properties between bulky and submicron materials due to the size effect [28].

Recently, poly(acrylonitrile) (PAN) and the electrospinning process have been frequently adopted as a precursor of the carbonaceous materials and a process for making composite electrodes, respectively, because of their well-established carbon nanofibers (CNFs) fabrication method [4,9–12,19,29–33]. Nevertheless, the electrochemical performances of PAN-based CNFs without metal or metal oxide additives were rarely investigated except for porous CNFs [34–36]. Moreover, the controllability of CNFs electrochemical performances by changing the thermal treatment was rarely

* Corresponding author. Tel.: +82 2 880 9096; fax: +82 2 883 8197.
E-mail address: woongryu@snu.ac.kr (W.-R. Yu).

0378-7753/$ – see front matter © 2011 Elsevier B.V. All rights reserved.
doi:10.1016/j.jpowsour.2011.10.030

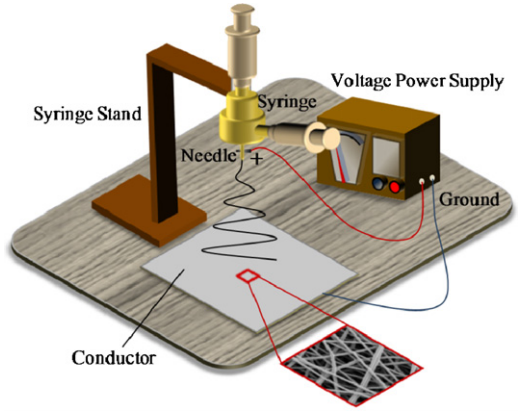

Fig. 1. Schematic diagram of co-axial electrospinning set-up.

studied [35], and the reported results were not consistent with those of bulky PAN-based anodes [27]. In this research, the hollow CNFs (HCNFs) were prepared using co-axial electrospinning of styrene-*co*-acrylonitrile (core) and poly(acrylonitrile) (shell) solutions and subsequent thermal treatments. Their microstructures were investigated as a function of carbonization temperatures and the correlation between the microstructures and the electrochemical performances of HCNFs were examined.

2. Experimental

Styrene-*co*-acrylonitrile (SAN, M_w = 120,000 g mol^{-1}, Cheil industries) was used as a sacrificial core material. Its acrylonitrile portion was 28.5 mol%. PAN (M_w = 200,000 g mol^{-1}, Misui chemical) was used as a shell material. *N*,*N*-Dimethylformamide (DMF, 99.5%, Deajung chemical) was used as a common solvent for both SAN and PAN. The concentrations of SAN and PAN were 30 and 20 wt%, respectively. The solution was then ultrasonicated for 5 h, and further stirred at 80 °C for 5 h.

A co-axial nozzle with two concentric cylinders was designed to make core/shell precursor nanofibers. The gauge needles were 17 and 22 for outer and inner cylinders, respectively. The co-axial electrospinning process is schematically shown in Fig. 1 and its parameters were set up as follows: applied voltage −18 kV, tip-to-collector distance – 15 cm, the flow rates of the inner and outer solutions – 0.5 and 1 ml h^{-1}, respectively. Core (SAN)/shell (PAN) precursor nanofibers were then thermally treated for the stabilization and carbonization of the PAN shell (see Fig. 2(a)). The stabilization of the PAN was conducted at 270–300 °C for 1 h under an air atmosphere, thus converting the linear PAN molecules to ladder polymers by cyclization and dehydrogenation [37]. The microstructure of carbonized PAN is strongly dependent on the carbonization temperature [38]. Subsequent carbonizations were carried out at 800, 1000, 1200, and 1600 °C (sample codes: 800, 1000, 1200, and 1600) for 1 h under a nitrogen atmosphere in order to investigate the effect of the carbonization temperature on the microstructures of HCNFs and their electrochemical performances. Here the temperature was increased at a rate of 10 °C min^{-1}. The structural evolution of the precursor nanofibers during the thermal treatment is schematically depicted in Fig. 2(b).

The tubular structures, morphologies, and atomic compositions of HCNFs were investigated using a field emission scanning electron microscope (FE-SEM) (SUPRA 55VP, Carl Zeiss). Their microstructures were investigated using a high resolution transmission electron microscope (HR-TEM, JEM-3000F). Raman spectroscopy (Ar laser, wave length: 514 nm, T64000, HORIBA) and wide angle X-ray diffraction (WAXD) (wave length: 0.154 nm, New D8 Advance, Bruker) were employed to characterize the carbonized structures of HCNFs. The surface area and porosity of HCNFs were characterized using nitrogen adsorption at 77 K using Brunauer–Emmett–Teller (BET) (Micromeritics ASAP2420).

A two-electrode 2032-type coin cells were employed to evaluate the electrochemical performance of HCNFs [39]. The anode slurry was prepared by mixing HCNFs (60 wt%), acetylene black (20 wt%, Alfa Aesar), and poly(vinylidene floride) (20 wt%, Alfa Aesar) in 1-methyl-2-pyrrolidinone (Alfa Aesar). The mixture (slurry) was then screen-printed onto a copper foil (Alfa Aesar) and dried. The mass of HCNFs in anodes were 1.020 (800), 0.966 (1000), 0.918 (1200), and 1.254 mg (1600), respectively. A lithium foil (Alfa Aesar) was used as the counter and reference electrode for a half-cell configuration. Glass fibers (Whatman) were used as the separator, while 1 M $LiPF_6$ in a mixed solution of propylene carbonate and diethyl carbonate (volume ratio 1:1, TSC Michigan) was used as the electrolyte. The coin-cells were assembled, crimped, and closed in an Ar-filled glove box. The electrochemical measurements were then performed at current densities of 50 mA g^{-1} for lithium insertion and extraction between 0.01 and 1.5 V.

3. Results and discussion

In order to fabricate electrochemically active materials, the SAN core/PAN shell nanofibers should be converted to carbonized structures. The cross-sections of carbonized HCNF in Fig. 3 demonstrates that each HCNF has a monotonic hollow shape resulted

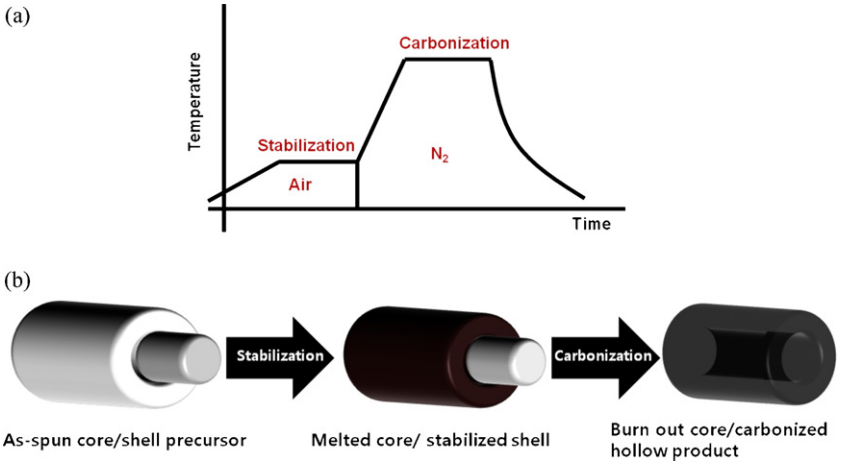

Fig. 2. (a) Schematic thermal treatment profile and (b) structural evolution during thermal treatment.

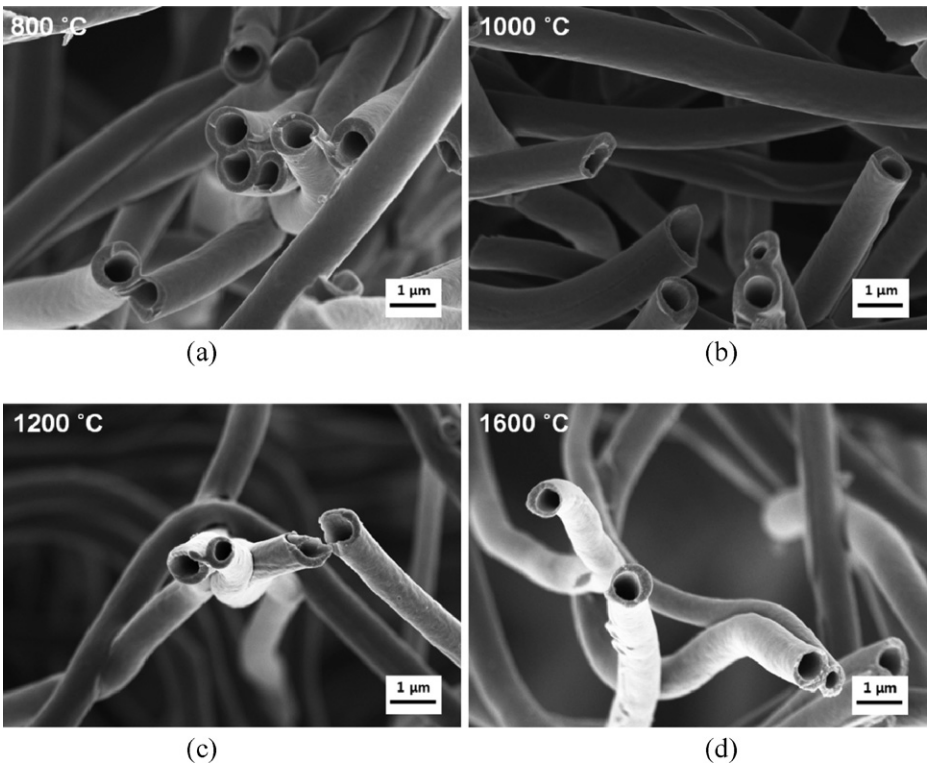

Fig. 3. FE-SEM images of HCNFs carbonized at various carbonization temperatures: (a) 800, (b) 1000, (c) 1200, and (d) 1600 °C.

from burning out the sacrificial core (SAN). Although PMMA and mineral oil were used in previous reports to make electrospun hollow or core/shell carbon fibers [4,40], SAN turned out to be a highly suitable sacrificial core because of its immiscibility with PAN/DMF solution and thermal sustainability during the stabilization process [41]. The overall diameters of HCNFs were examined to investigate the effects of the carbonization temperature (see Fig. 4). The average diameters decreased with increasing carbonization temperature up to 1200 °C, and then it slightly increased at 1600 °C. This phenomenon could be understood by considering the microstructural evolution of HCNFs, including ladder formation and combination into graphitic layers [42].

HCNFs were characterized using WAXD, Raman spectroscopy and BET. The WAXD curves demonstrate the successful formation of carbonized microstructure. In Fig. 5(a), the curves have the three

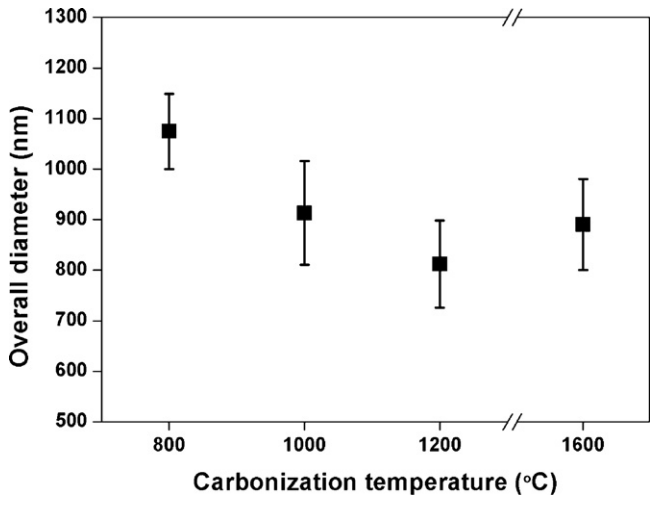

Fig. 4. Diameter changes of HCNFs according to carbonization temperature.

equatorial peaks: primary ((0 0 2), around $2\theta = 25^\circ$) and secondary ((1 0 l), around $2\theta = 43^\circ$) for the carbon graphitic layers. The d_{002} values calculated from the primary peaks of the WAXD curves gradually diminished, e.g., 0.361 nm (1000), 0.359 nm (1200), and 0.354 nm (1600), except 0.353 nm (800). The calculated d_{002} values were larger than that of graphite (0.335 nm), implying that the microstructure of HCNFs is a turbostratic carbon structure with a slightly mismatched layer-sequence [43]. The secondary peaks were sharply developed as the carbonization temperature increased, while the tertiary peak (0 0 4) of the material carbonized at 1600 °C slightly emerged at around $2\theta = 53^\circ$. Raman spectroscopy offers further evidence confirming the carbonized structure in the HCNFs (Fig. 5(b)). In general, Raman spectra of carbonaceous materials contain two peaks called D and G peaks. The D peak near 1350 cm^{-1} is related to the breaking of symmetry caused by structural disorders and defects, while the G peak near 1580 cm^{-1} represents the in-plane tangential stretch vibration mode (E_{2g}) of the graphite sheet [44]. The peaks were narrowly developed as the carbonization temperature increased. Moreover, the I_D/I_G ratios from the Gaussian fitting curves decreased from 1.46 for 800 °C to 0.77 for 1600 °C, demonstrating that more of the graphitic structure was developed with increasing carbonization temperature. The surface area and pore distribution characterized by BET have the same order of magnitudes as those of solid CNFs (see Table 1) [45,46]. The nitrogen adsorption isotherm in Fig. 6(a) shows the

Table 1
The summary of nitrogen adsorption properties of HCNFs.

Carbonization temperature (°C)	BET SSA ($m^2\ g^{-1}$)	Total pore volume ($cm^3\ g^{-1}$)	Average pore volume 4V/A (nm)
800	20.35	0.03317	6.52
1000	13.18	0.02746	8.33
1200	15.83	0.04307	10.88
1600	6.20	0.07531	11.00

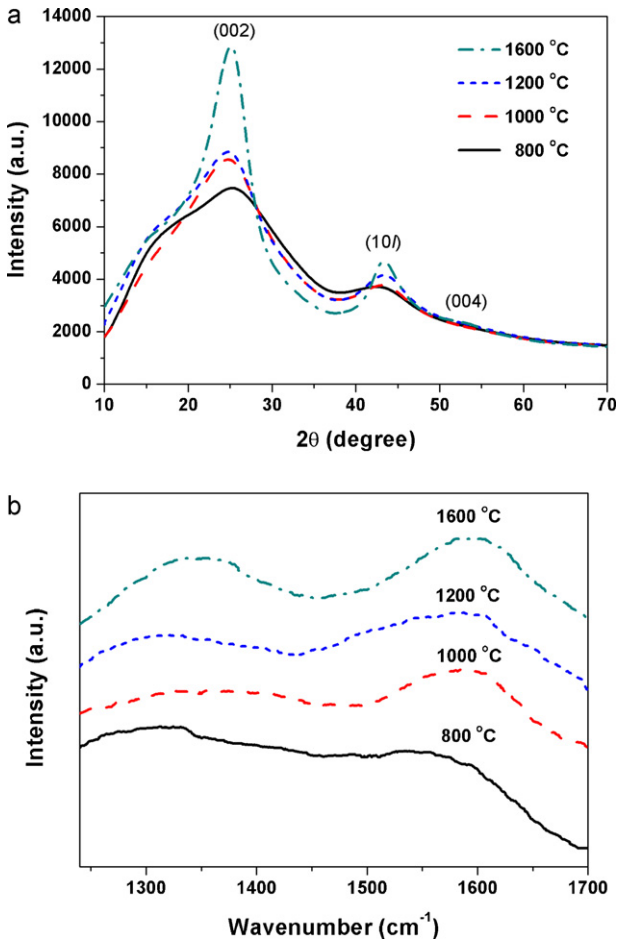

Fig. 5. (a) WAXD curves and (b) Raman spectra of HCNFs according carbonization temperature.

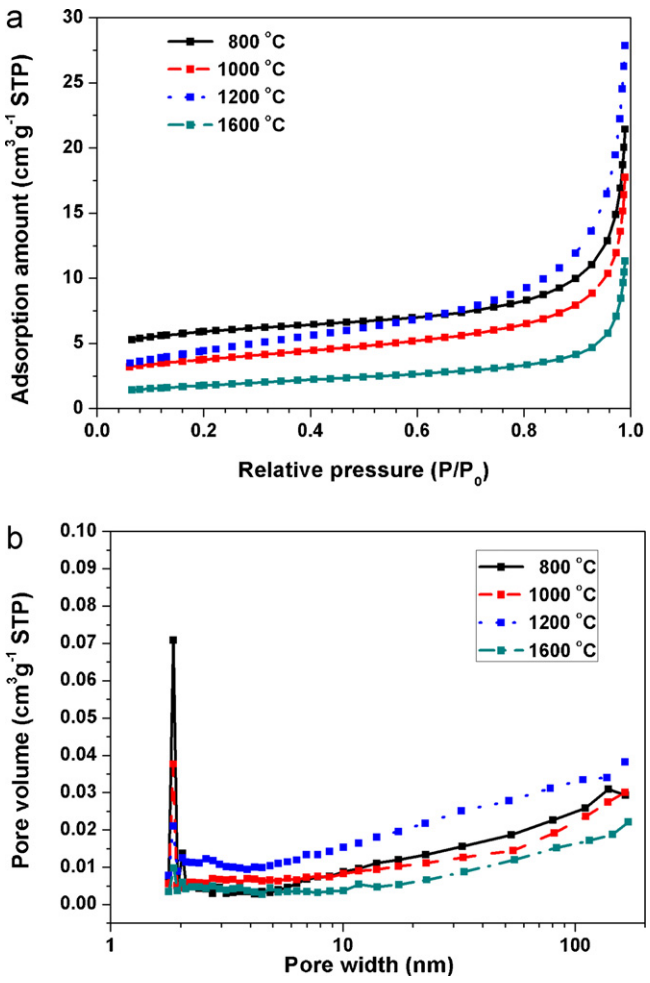

Fig. 6. (a) The nitrogen adsorption isotherms of HCNFs and (b) their pore size distributions.

typical behavior of non-porous carbons (Type III isotherm according to IUPAC classification [47]). Meanwhile, micropores (<2 nm) were developed more significantly than meso (>2 nm and <50 nm) or macropores (>50 nm). As shown in Fig. 6(b), micropores were dominant in all HCNFs, and their amounts decreased according to the carbonization temperature. Overall pore volume decreased according to the carbonization temperature, which were related to closed micropores formed at higher carbonization temperature [24].

The HR-TEM images and electron diffraction patterns of HCNFs in Fig. 7 demonstrates that the microstructures of HCNFs were transformed into more ordered structures in a qualitative manner. Previous studies have been dedicated to investigating the crystallite thickness change of micro and nanoscale carbon nanofibers using Scherrer's formula [48–50], while Arshad et al. [38] investigated the crystallite thickness using HR-TEM images and showed good agreement with the values from Scherrer's formula. Therefore, the crystallite dimensions were measured in a quantitative manner by focusing on the crystallite thickness (L_c, the number of layers) and size (L_a) (see Table 2). Both the crystallite size and thickness increased as the carbonization temperature increased. The condensation reaction that formed the turbostratic layers is believed to result in clustering and interconnecting of the mosaic domains by tilting and twisting [51]. The enlargement of L_a from 800 to 1000 °C was considerable. In this range, the broadness of turbostratic layers is preferred compared to the stacking of the turbostratic layers [48,51]. The stacking of the turbostratic layers was stimulated by increasing the carbonization temperature. The decreases of d_{002} from Figs. 5(a) and 7 were another significant change which demonstrated the development of more compact and more perfect microstructures by de-wrinkling the turbostratic layers. The diffracted concentric ring patterns (i.e. the inner, medium, and outer circles corresponded to (0 0 2), (1 0 *l*), and (0 0 4), respectively) signify the sample that was carbonized at a higher temperature, implying the formation of randomly oriented poly-crystallites. The crystallite dimensions were strictly governed by the carbonization temperatures, while the orientation of crystallites was isotropic. As a container material of metallic or ceramic materials, the random orientation of crystallites could yield a predictive buffering behavior. The atomic compositions showed the successful dehydrogenation during the stabilization confirming reasonable residual N and O contents (14.7 and 3.4% (800), 8.3 and 5.3% (1000), 4.6 and 1.7% (1200), and 8.7 and 6.7% (1600), respectively) compared to a previous report [42]. The distinctive tendencies, however, were not observed, and the carbon contents in HCNFs were higher than 80% for every sample.

Galvanostatic charge–discharge tests were conducted to assess the electrochemical performance of HCNFs. The charge–discharge curves of HCNF anodes between 0.01 and 1.5 V at a current of 50 mA g^{-1} were shown in Fig. 8(a–d). On the 1st charge curve, two inflection points at about 0.75 and 0.2 V are observed and they represent the formation of solvated Li intercalation compounds followed by solvent decomposition and the formation of Li_xC_6, respectively [52]. The former inflection point corresponds to the irreversible capacity, and the reaction of solvated Li intercalation is

Table 2
The microstructures and atomic contents of HCNFs according to carbonization temperature.

Carbonization temperature (°C)	d_{002} (nm)	Crystallite thickness (the number of layers, L_c)	Crystallite size (L_a, nm)	Atomic contents (C:N:O:H, wt%)
800	0.362	3.3 (0.9)	1.28 (0.42)	81.9:14.7:3.4:0
1000	0.352	4.6 (0.8)	4.54 (0.87)	86.4:8.3:5.3:0
1200	0.347	5.1 (1.7)	5.83 (1.87)	93.7:4.6:1.7:0
1600	0.341	8.1 (1.6)	10.62 (3.69)	84.6:8.7:6.7:0

The parenthesis represents the standard deviation of the values.

inhibited by the formation of the SEI layer for the 1st cycle, while the latter inflection is reversibly repeated in subsequent cycles. The electrochemical performances of carbonaceous materials have been recognized as a function of their microstructure [26,27]. The charge and discharge capacities of subsequent cycles rapidly converged with higher carbonization temperatures due to reduced structural imperfection.

The reduction of both initial capacities and initial irreversible capacity as a function of the carbonization temperature can be clearly seen in Fig. 9. Both the reversible and irreversible capacities at the 1st cycle of HCNFs carbonized at 800 °C are the largest (545 and 477 mAh g^{-1}, respectively), and the capacities gradually decreased to 266 and 142 mAh g^{-1} as the carbonization temperature increased up to 1600 °C. The insufficient development of the carbonized microstructure at lower temperatures is considered to be the cause of the large fraction of the irreversible capacity, because the reversible intercalation of Li ions occurs only in graphitic (or turbostratic) sheets [52]. The fraction of the irreversible capacities decreased and became saturated at around 38%. The reduction of the irreversible capacity is meaningful not only by itself but also in the fabrication of the composite anode. For instance, if a composite anode consists of Si 25 wt% and HCNF (1600) 75 wt%, the capacity is estimated over 1000 mAh g^{-1}. Therefore, the irreversible capacity of HCNF (1600) is only 11% of the postulated composite materials. Meanwhile, the crystallite enlargement (increased size and thickness) with increasing carbonization temperature results in the lowered reversible capacities. This is due to the reduction of the single graphitic layers fraction by progressing into the graphitic layers stacking in accordance to the carbonization temperature increase. Dahn et al. [53] postulated and proved that controlling the capacity as a function of the single graphitic layers fraction enables one to double the capacity by alloying both sides. This phenomenon coincide with previous works on PAN-based carbon fibers [27] and mesocarbon microbeads (MCMBs) [26]. The

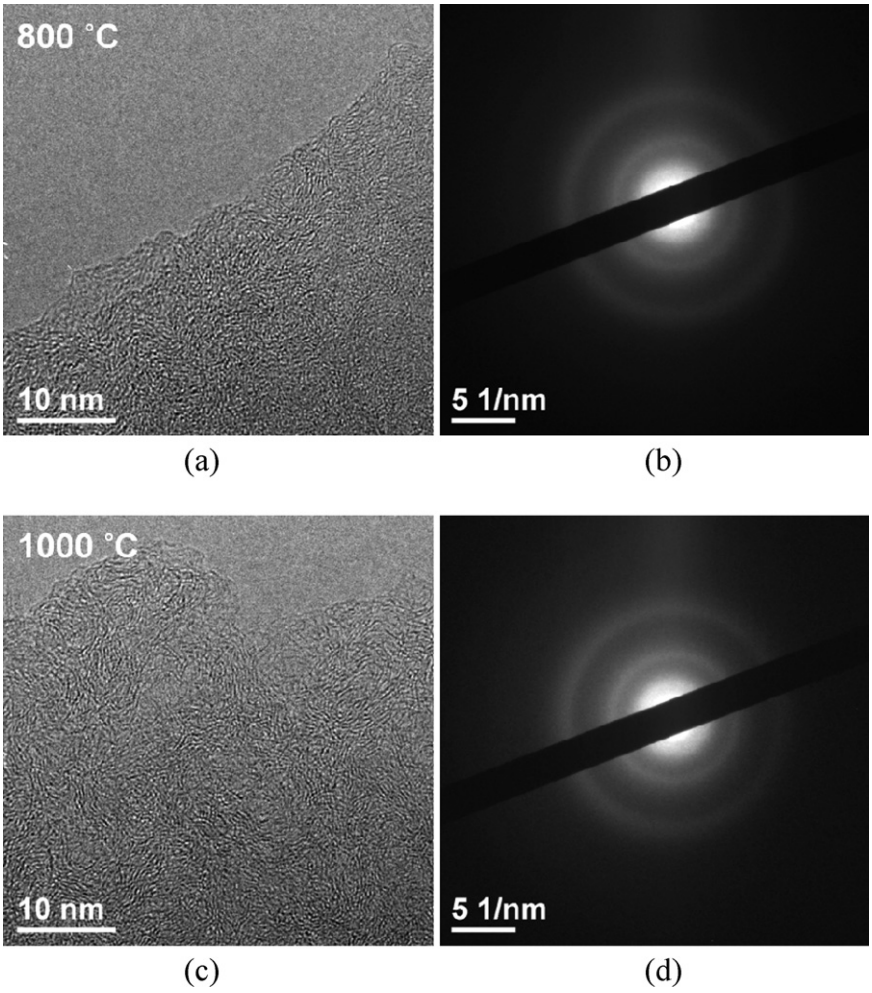

Fig. 7. HR-TEM images and electron diffraction pattern of HCNFs according to carbonization temperature. (a and b) 800, (c and d) 1000, (e and f) 1200, and (g and h) 1600 °C.

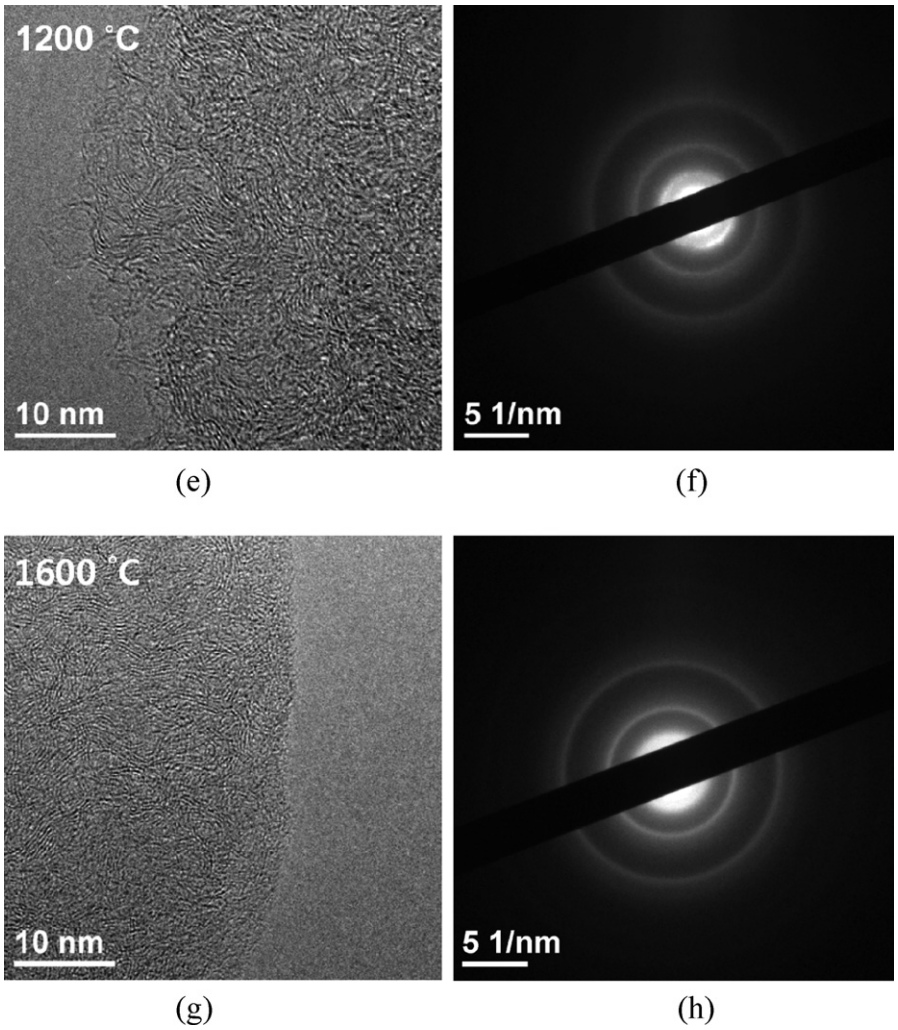

Fig. 7. (*continued*).

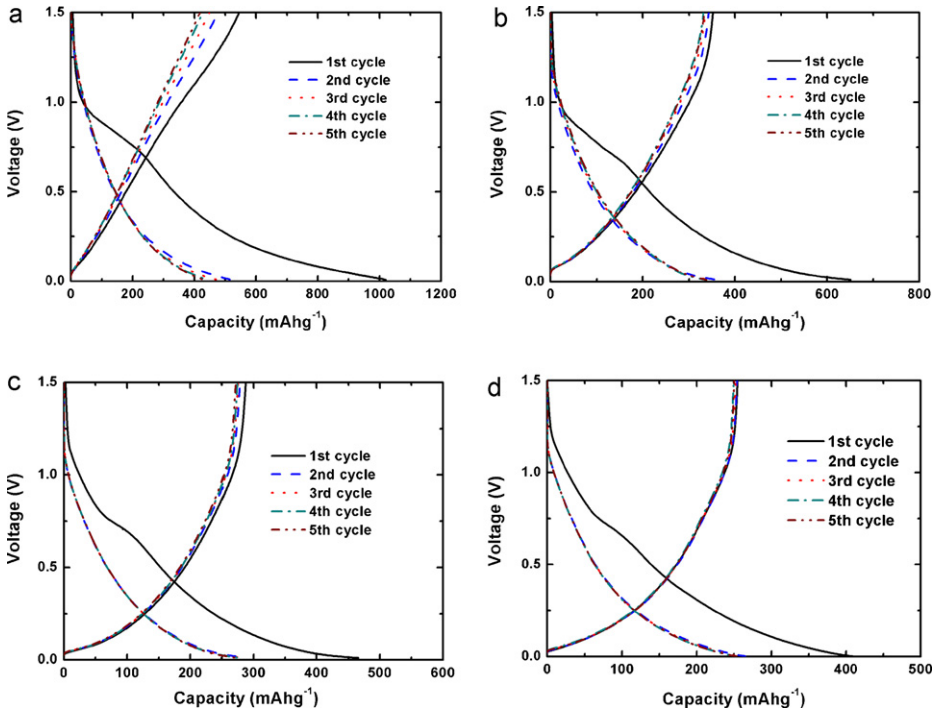

Fig. 8. Voltage profiles of HCNFs: (a–d) carbonized at 800, 1000, 1200, and 1600 °C.

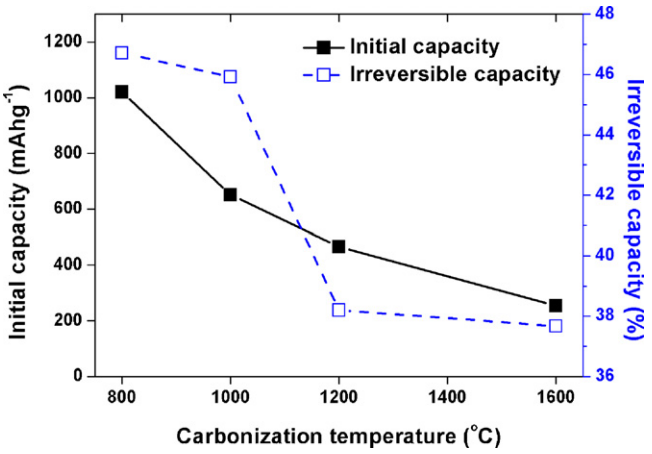

Fig. 9. Initial and irreversible capacities of HCNFs on carbonization temperature change.

cycling performances in Fig. 10 demonstrate that the reversible capacities and coulombic efficiencies were converged within several cycles. After 10 cycles, the specific reversible capacities were converged to 390, 334, 273, and 243 mAh g^{-1} in accordance to their carbonization temperature (800–1600 °C), while the coulombic efficiencies commonly reached 99.39, 99.32, 99.35, and 99.51%, respectively. Such higher coulombic efficiencies suggest the

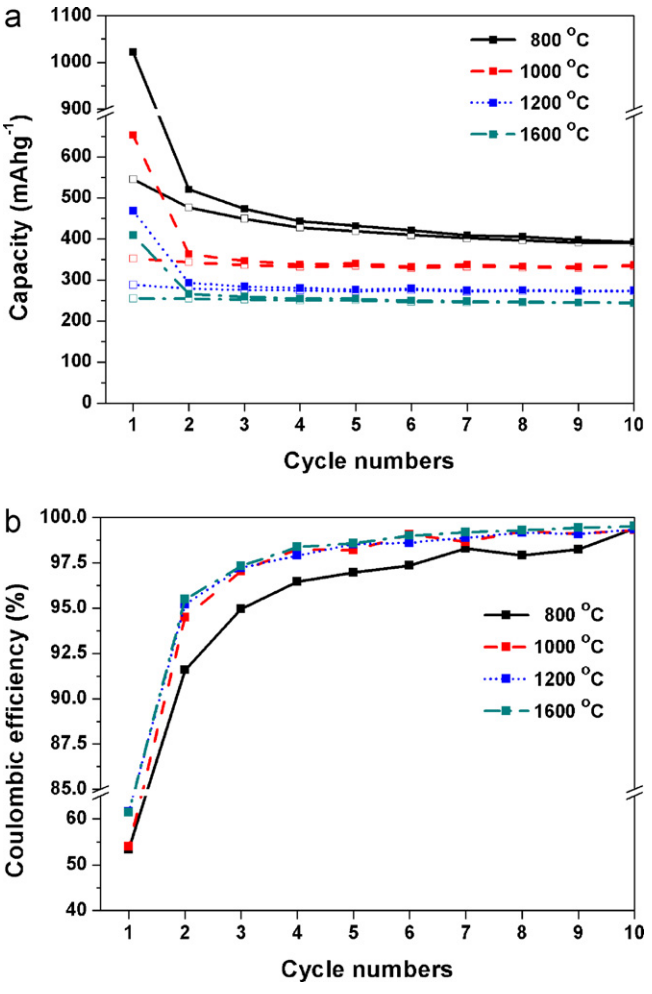

Fig. 10. Cycling performance of HCNFs at a constant current density of 50 mA g^{-1}: (a) charge–discharge capacity and (b) coulombic efficiency.

Table 3
The reversible discharge capacities on the current densities for 2nd cycles.

Carbonization temperature (°C)	Reversible discharge capacities (mAh g^{-1})		Differences of discharge capacities (mAh g^{-1})
	On 50 mA g^{-1}	On 200 mA g^{-1}	
800	517.7	436.4	81.3
1000	361.6	344.7	16.9
1200	278.5	250.0	28.5
1600	266.0	256.6	9.4

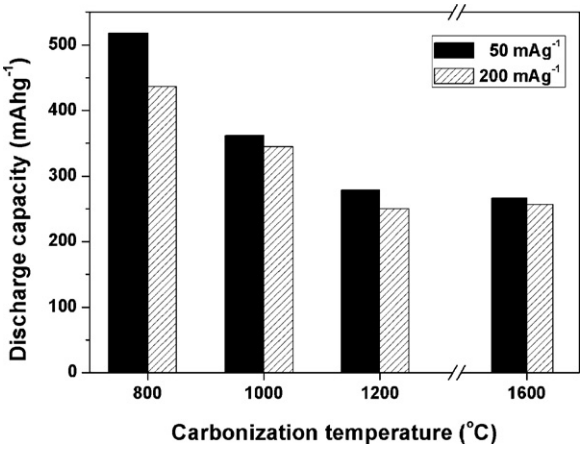

Fig. 11. Discharge capacity vs. discharge rate for the second cycle for HCNFs.

applicability of HCNFs as a metal or metal oxide container material. To be utilized as a container material for Si and Sn, the electrochemical performances should be stably maintained at higher current densities (e.g. 0.1 C of crystalline Si: ~400 mA g^{-1}). Thus, the reversible discharge capacities on the current densities (50 and 200 mA g^{-1}) for 2nd cycles were investigated as shown in Fig. 11. Although the reversible capacities decreased as the current densities increased, the differences between the differences were not significant (i.e., the percent differecences were 15.7 (800), 4.6 (1000), 10.2 (1200), and 3.5% (1600), respectively) (see Table 3). This clearly demonstrates the feasibility for this material to act as a composite anode.

4. Conclusions

Various HCNFs are prepared as carbon shells which can contain metallic or ceramic materials for electrochemical applications. The HCNFs are successfully fabricated by using a co-axial electrospinning technique and SAN core/PAN shell composition. Their overall diameters and hollowed morphologies are observed using FE-SEM. The degree of microstructural perfection as the carbonization temperature increased is qualitatively and quantitatively examined by WAXD, Raman spectroscopy, and HR-TEM. The electrochemical performances of the HCNFs are investigated by using Galvanostatic charge–discharge testing. Both the reversible and irreversible capacities decrease, while the convergence of voltage profiles accelerates according to increased carbonization temperature. The initial capacities and initial irreversible capacity rate are strongly related to the microstructure. The cycling performances are quite stable, and the coulombic efficiencies exceed 99.3% (99.51% for 1600 °C). The reversible discharge capacities are slightly reduced even though four times higher current density is supplied. The stable and tunable electrochemical performances of HCNFs can be used to fabricate composite electrodes containing metallic or ceramic active materials.

Acknowledgement

This research was supported by Basic Science Research Program through the National Research Foundation of Korea (NRF) funded by the Ministry of Education, Science and Technology (2010-0022633).

References

[1] X. Ji, K.T. Lee, L.F. Nazar, Nat. Mater. 8 (2009) 500–506.
[2] Y. Yang, M.T. McDowell, A. Jackson, J.J. Cha, S.S. Hong, Y. Cui, Nano Lett. 10 (2010) 1486–1491.
[3] H. Wang, Y. Yang, Y. Liang, J.T. Robinson, Y. Li, A. Jackson, Y. Cui, H. Dai, Nano Lett. 11 (2011) 2644–2647.
[4] Y. Yu, L. Gu, C. Wang, A. Dhanabalan, P.A. van Aken, J. Maier, Angew. Chem. Int. Ed. 48 (2009) 6485–6489.
[5] M. Yoshio, H. Wang, K. Fukuda, T. Umeno, N. Dimov, Z. Ogumi, J. Electrochem. Soc. 149 (2002) A1598–A1603.
[6] P. Poizot, S. Laruelle, S. Grugeon, L. Dupont, J.M. Tarascon, Nature 407 (2000) 496–499.
[7] U. Kasavajjula, C. Wang, A.J. Appleby, J. Power Sources 163 (2007) 1003–1039.
[8] H.-R. Jung, W.-J. Lee, J. Electrochem. Soc. 158 (2011) A644–A652.
[9] L. Ji, X. Zhang, Carbon 47 (2009) 3219–3226.
[10] L. Ji, X. Zhang, Electrochem. Commun. 11 (2009) 1146–1149.
[11] L. Ji, X. Zhang, Electrochem. Commun. 11 (2009) 795–798.
[12] L. Wang, C.X. Ding, L.C. Zhang, H.W. Xu, D.W. Zhang, T. Cheng, C.H. Chen, J. Power Sources 195 (2010) 5052–5056.
[13] X.-W. Zhang, P.K. Patil, C. Wang, A.J. Appleby, F.E. Little, D.L. Cocke, J. Power Sources 125 (2004) 206–213.
[14] L.-F. Cui, Y. Yang, C.-M. Hsu, Y. Cui, Nano Lett. 9 (2009) 3370–3374.
[15] H. Kim, J. Cho, Nano Lett. 8 (2008) 3688–3691.
[16] J.Y. Lee, R. Zhang, Z. Liu, Electrochem. Solid State Lett. 3 (2000) 167–170.
[17] J. Read, D. Foster, J. Wolfenstine, W. Behl, J. Power Sources 96 (2001) 277–281.
[18] W.-M. Zhang, J.-S. Hu, Y.-G. Guo, S.-F. Zheng, L.-S. Zhong, W.-G. Song, L.-J. Wan, Adv. Mater. 20 (2008) 1160–1165.
[19] Y. Yu, L. Gu, C. Zhu, P.A. van Aken, J. Maier, J. Am. Chem. Soc. 131 (2009) 15984–15985.
[20] G. Cui, Y.-S. Hu, L. Zhi, D. Wu, I. Lieberwirth, J. Maier, K. Müllen, Small 3 (2007) 2066–2069.
[21] S. Flandrois, B. Simon, Carbon 37 (1999) 165–180.
[22] Y. Wu, S. Fang, Y. Jiang, J. Power Sources 75 (1998) 201–206.
[23] M. Endo, C. Kim, K. Nishimura, T. Fujino, K. Miyashita, Carbon 38 (2000) 183–197.
[24] E. Buiel, A.E. George, J.R. Dahn, J. Electrochem. Soc. 145 (1998) 2252–2257.
[25] M. Endo, Y. Nishimura, T. Takahashi, K. Takeuchi, M.S. Dresselhaus, J. Phys. Chem. Solids 57 (1996) 725–728.
[26] A. Mabuchi, K. Tokumitsu, H. Fujimoto, T. Kasuh, J. Electrochem. Soc. 142 (1995) 1041–1046.
[27] J.K. Lee, K.W. An, J.B. Ju, B.W. Cho, W.I. Cho, D. Park, K.S. Yun, Carbon 39 (2001) 1299–1305.
[28] K.Y. Hwang, S.-D. Kim, Y.-W. Kim, W.-R. Yu, Polym. Test. 29 (2010) 375–380.
[29] O. Toprakci, L. Ji, Z. Lin, H.A.K. Toprakci, X. Zhang, J. Power Sources 196 (2011) 7692–7699.
[30] Z. Lin, L. Ji, M.D. Woodroof, X. Zhang, J. Power Sources 195 (2010) 5025–5031.
[31] Y. Liang, L. Ji, B. Guo, Z. Lin, Y. Yao, Y. Li, M. Alcoutlabi, Y. Qiu, X. Zhang, J. Power Sources 196 (2011) 436–441.
[32] L. Wang, Y. Yu, P.C. Chen, D.W. Zhang, C.H. Chen, J. Power Sources 183 (2008) 717–723.
[33] Y.-W. Ju, G.-R. Choi, H.-R. Jung, W.-J. Lee, Electrochim. Acta 53 (2008) 5796–5803.
[34] L. Ji, Z. Lin, A.J. Medford, X. Zhang, Carbon 47 (2009) 3346–3354.
[35] L. Ji, Y. Yao, O. Toprakci, Z. Lin, Y. Liang, Q. Shi, A.J. Medford, C.R. Millns, X. Zhang, J. Power Sources 195 (2010) 2050–2056.
[36] L. Ji, X. Zhang, Nanotechnology 20 (2009) 155705.
[37] E. Fitzer, D.J. Müller, Carbon 13 (1975) 63–69.
[38] S.N. Arshad, M. Naraghi, I. Chasiotis, Carbon 49 (2011) 1710–1719.
[39] Y.S. Jung, S. Lee, D. Ahn, A.C. Dillon, S.-H. Lee, J. Power Sources 188 (2009) 286–291.
[40] E. Zussman, A.L. Yarin, A.V. Bazilevsky, R. Avrahami, M. Feldman, Adv. Mater. 18 (2006) 348–353.
[41] B.-S. Lee, W.-R. Yu, 14th European Conference on Composite Materials, Budapest, Hungary, 2010.
[42] M.S.A. Rahaman, A.F. Ismail, A. Mustafa, Polym. Degrad. Stab. 92 (2007) 1421–1432.
[43] A. Ōya, H. Marsh, J. Mater. Sci. 17 (1982) 309–322.
[44] B.-S. Lee, W.-R. Yu, Macromol. Res. 18 (2010) 162–169.
[45] D.-K. Kim, S. Park, B. Kim, B. Chin, S. Jo, D. Kim, Macromol. Res. 13 (2005) 521–528.
[46] J.S. Im, S.-J. Park, T.J. Kim, Y.H. Kim, Y.-S. Lee, J. Colloid Interface Sci. 318 (2008) 42–49.
[47] Z. Ryu, J. Zheng, M. Wang, B. Zhang, Carbon 37 (1999) 1257–1264.
[48] J. Liu, P.H. Wang, R.Y. Li, J. Appl. Polym. Sci. 52 (1994) 945–950.
[49] F. Liu, H. Wang, L. Xue, L. Fan, Z. Zhu, J. Mater. Sci. 43 (2008) 4316–4322.
[50] E. Zussman, X. Chen, W. Ding, L. Calabri, D.A. Dikin, J.P. Quintana, R.S. Ruoff, Carbon 43 (2005) 2175–2185.
[51] S. Fonton, A. Oberlin, M. Inagaki, J. Mater. Sci. 15 (1980) 909–917.
[52] J.S. Kim, Y.T. Park, J. Power Sources 91 (2000) 172–176.
[53] J.R. Dahn, T. Zheng, Y. Liu, J.S. Xue, Science 270 (1995) 590–593.